International Journal of Heat and Mass Transfer 52 (2009) 5390–5401

Contents lists available at ScienceDirect

International Journal of Heat and Mass Transfer

journal homepage: www.elsevier.com/locate/ijhmt

CFD modeling of mass transfer in annular reactors

J. Esteban Duran, Fariborz Taghipour, Madjid Mohseni *

Department of Chemical and Biological Engineering, The University of British Columbia, 2360 East Mall, Vancouver, BC, Canada V6T 1Z3

ARTICLE INFO

Article history:
Received 16 January 2009
Received in revised form 10 July 2009
Available online 14 August 2009

Keywords:
CFD
Modeling
Mass transfer
Annular reactor
Turbulence model
Low Reynolds number k–ε model

ABSTRACT

A computational fluid dynamics (CFD) investigation of single-phase flow mass transfer prediction in annular reactors was conducted. Different hydrodynamic models including laminar, standard k–ε, realizable k–ε, Reynolds stress (RSM), and the Abe-Kondoh-Nagano (AKN) (a low Reynolds number turbulence model) were evaluated against experimental data in terms of their mass transfer predication capabilities. The laminar model predicted successfully the average mass transfer in the flows under laminar regime ($Re < 1500$). Among the four evaluated turbulence models, the AKN model provided a better prediction of the average mass transfer rates in the systems when operated both under transitional and turbulent conditions ($3000 < Re < 11000$). The RSM performed very similarly to the AKN model, except for the entrance region of the reactors where it predicted lower mass transfer rates. These results make the AKN and RSM models very attractive to be integrated in CFD-based simulations of turbulent annular reactors.

1. Introduction

The annular reactor geometry has been increasingly finding many applications in chemical engineering processes. Some of the most common configurations include tube wall reactors [1,2], membrane reactors [3], electrochemical reactors [4], dialyzers [5], and immobilized photocatalytic reactors [6,7]. Despite their potential success and applications, mass transfer limitations could be an issue in these reactors depending on the kinetics, operating conditions, and the geometrical properties of the system. Hence, when modeling these reactors, an accurate prediction of fluid flow and thus, local mass transfer is needed.

Most of the previous studies on mass transfer in annular reactors reported in the open literature have concentrated on obtaining correlations of dimensionless numbers for different configurations and operating conditions. Rai et al. [8] compiled several correlations for both developed and developing boundary layers under laminar and turbulent flow conditions. More recently, Mobarak et al. [9] measured the rates of solid–liquid mass transfer at the inner surface (smooth and rough) of an annular duct by the electrochemical technique under developing flow conditions. Table 1 provides a list of some of the correlations available in the literature. Even though the design of annular reactors has relied for many years on the use of such correlations, they present the disadvantage of being applicable only to a specific reactor configuration operated under a certain range of hydrodynamic conditions. Besides, this type of design correlations does not take into account local effects. Moreover, the non-idealities introduced by scaling up of the lab or pilot-scale equipment are difficult, if not impossible, to predict empirically [13].

A better approach to estimate mass transfer in annular reactors is finding suitable models that allow predicting the concentration fields inside the reactor. Several researchers have taken this approach; for instance, Houzelot and Villermaux [14] performed a numerical simulation of radial diffusional mass transfer in a fluid flowing in fully developed laminar flow in a reactor in which a first order heterogeneous reaction was taking place at the wall. The simulation results were in excellent agreement with those yielded by the experiments and the investigation revealed that annular reactors exhibit a mass transfer efficiency which is noticeably higher than that of empty tubes. Other researchers have proposed and evaluated several mathematical models which included mass transfer in annular reactors used for different applications, but their systems were limited either to laminar, or to fully developed turbulent flow conditions [10,11,15–21]. Practical annular reactors, however, often do not have an entrance length to assure a fully developed flow. In fact, in most of the cases, developing flow is desirable since it gives rise to enhanced mass transfer. In this sense, inlet and outlet port configurations, so as internal accessories (e.g., internal baffles) usually play an important role in improving mass transfer performance of the reactor.

Mass transfer modeling under developing flow condition is a complex task. However, the application of computational fluid dynamics (CFD) has demonstrated to be a very effective approach

* Corresponding author. Tel.: +1 604 822 0047; fax: +1 604 822 6003.
E-mail address: mmohseni@chbe.ubc.ca (M. Mohseni).

0017-9310/$ - see front matter © 2009 Elsevier Ltd. All rights reserved.
doi:10.1016/j.ijheatmasstransfer.2009.07.004

Nomenclature

A	area of mass transfer (m^2)
a	annulus diameter ratio, d_1/d_2 (dimensionless)
C	concentration of benzoic acid (mol m^{-3})
D_m	molecular diffusivity of species k in the mixture (m^2 s^{-1})
D_t	eddy (or turbulent) diffusivity for species concentration (m^2 s^{-1})
d	diameter (m)
h_m	average mass transfer coefficient (m s^{-1})
h	local mass transfer coefficient (m s^{-1})
J_k	diffusive flux of species k (kg s^{-1} m^{-2})
L	mass transfer section length (m)
m_k	mass fraction of species k (dimensionless)
m'_k	fluctuating mass fraction of species k (dimensionless)
P	pressure (Pa)
Q	flow rate (m^3 s^{-1})
Re	Reynolds number (dimensionless)
Re_y	wall-distance-based turbulent Reynolds number (dimensionless)
Sc_t	turbulent Schmidt number (dimensionless)
Sh_{av}	Sherwood number based on the average mass transfer coefficient (dimensionless)
t	elapsed time (s)
U	velocity (m s^{-1})
u	fluctuating flow velocity (m s^{-1})
V	total volume of liquid (m^3)
X	non-dimensional axial position, $4x(1-a)/(\mathrm{Re}\ d_2)$
x	axial position (m)
y^+	non-dimensional distance from the wall (dimensionless)

Greek symbols

μ_t	turbulent viscosity (m^2 s^{-1})
ρ	density (kg m^{-3})
τ	viscous stress tensor (N m^{-2})
φ	function defined as $[(1-a)/a]\,[1/2-(a^2/(1-a^2))\ln(1/a)]\,/\,[((1+a^2)/(1-a^2))\ln(1/a)-1]$

Subscripts

0	initial condition ($t = 0$)
1	inner annular cylinder
2	outer annular cylinder
a	adjacent to the wall
b	bulk value
e	equivalent or hydraulic
i	inlet condition
o	outlet condition
sat	saturation condition
x	along the axial position

for tackle this challenge. Taghipour and Mohseni [6] and Mohseni and Taghipour [22] applied computational fluid dynamics (CFD) and simulated laminar flow annular photocatalytic reactors treating chlorinated VOCs. The CFD-models were capable of predicting the reactor performance and provided insight into the concentration gradients of the species in the reactor. For the case of annular reactors operating under developing turbulent flow regime, little modeling work has been done. Sozzi and Taghipour [23] performed a detailed CFD simulation of the hydrodynamics of two annular photoreactor configurations (concentric and normal inlets), and evaluated the results with the velocity profiles from particle imagine velocimetry (PIV). Under the evaluated operational conditions, the realizable k–ε and the Reynolds stress model (RSM) turbulence models displayed the best overall match to the experimental PIV measurements. Even though this investigation brought an important outcome in terms of recommending appropriate turbulence models for computing the fluid velocity field inside annular reactors, further investigation is needed to assess their applicability to mass transfer modeling. Since the wall-liquid mass transfer phenomenon takes place almost completely within the near-wall region, near-wall modeling significantly impacts the validity of numerical solutions and requires experimental evaluation. To the authors' knowledge, no research has been performed on modeling and experimentally evaluating mass transfer of transient and turbulent flow with simultaneous development of velocity and concentration boundary layers in commonly used annular reactor configurations.

This research has focused on applying CFD for modeling single-phase liquid fluid flow and mass transfer phenomena in commercial-type annular reactors. CFD allows for an in-depth analysis of the fluid mechanics, local mass transfer, and other physicochemical processes occurring in chemical reactors, thereby offering the possibility of achieving an improved performance, a better reliability, and a more confident scale-up of the equipment. The aim of this work was to carry out a comprehensive CFD study in which simulation results obtained using different hydrodynamic models were evaluated with experimental measurements of external mass transfer in annular reactors. The case of mass transfer from the inner surface of the outer tube (at constant concentration) was analyzed. The experimental determination of the mass transfer rates was achieved by coating the inner wall with benzoic acid (as a model chemical) and then measuring the dissolution of the slightly soluble acid into the flow stream. Two commonly used annular reactor configurations were studied: with the inlet normal (U-shape) and parallel (L-shape) to the main reactor body. Commercial CFD code Fluent® 6.3.26 was used to perform the simulations.

Table 1
Some correlations reported in the literature for mass transfer in annuli.

Hydrodynamic condition	Source	Correlation	Condition	Eq. no.
Laminar flow				
Fully developed	[10]	$Sh_{av} = 1.614(\mathrm{Re}Sc\varphi d_e/L)^{1/3}$		(1)
Developing	[9]	$Sh_{av} = 1.029Sc^{1/3}\mathrm{Re}^{0.55}(d_e/L)^{0.472}$		(2)
	[11]	$Sh_{av} = 0.66Sc^{1/3}(\mathrm{Re}\varphi d_e/L)^{0.52}$	$X \leqslant 42\times10^{-4}$	(3)
		$Sh_{av} = 1.56Sc^{1/3}(\mathrm{Re}\varphi d_e/L)^{0.34}$	$X \geqslant 42\times10^{-4}$	(4)
	[12]	$Sh_{av} = 2.703(\mathrm{Re}Sc\varphi d_e/L)^{1/3}$		(5)
Turbulent flow				
Fully developed	[10]	$Sh_{av} = 0.276Sc^{1/3}\mathrm{Re}^{0.58}(d_e/L)^{1/3}$	$L/d_e < 2$	(6)
		$Sh_{av} = 0.023Sc^{1/3}\mathrm{Re}^{0.8}$	$L/d_e > 2$	(7)
	[8]	$Sh_{av} = 0.027Sc^{1/3}\mathrm{Re}^{0.8}(d_2/d_1)^{0.53}$		(8)
	[4]	$Sh_{av} = 0.145Sc^{1/3}\mathrm{Re}^{2/3}(d_e/L)^{0.25}$	$L/d_e < 7.5$	(9)
Developing	[9]	$Sh_{av} = 0.095Sc^{0.33}\mathrm{Re}^{0.85}(d_e/L)^{0.472}$	$6.8 < L/d_e < 34.4$	(10)
	[12]	$Sh_{av} = 0.305Sc^{1/3}\mathrm{Re}^{2/3}(\varphi d_e/L)^{1/3}$		(11)
	[8]	$Sh_{av} = 0.032Sc^{1/3}\mathrm{Re}^{0.8}(1+(d_e/L)^{2/3})(d_2/d_1)^{0.53}$	$L/d_e < 7$	(12)

2. CFD modeling

2.1. Governing equations

In the present study, it is assumed that the fluid (water) is Newtonian, incompressible, isothermal, non-reactive, with constant physical properties and under turbulent steady state flow. Under these assumptions and following the Reynolds averaged Navier–Stokes (RANS) turbulence modeling approach [24], the CFD model involves solving the continuity equation (13), Reynolds average Navier–Stokes equation (14) and time-average conservation of species equation (15) which are expressed as

$$\nabla \cdot (\overline{U}) = 0 \tag{13}$$

$$\nabla \cdot (\rho \overline{U}\overline{U} + \rho \overline{u}\overline{u}) = -\nabla \overline{P} - \nabla \cdot \bar{\tau} \tag{14}$$

$$\nabla \cdot (\rho \overline{U}\overline{m_k} + \rho \overline{u m'_k}) = -\nabla \cdot \overline{J_k} \tag{15}$$

where the overbar indicates a time-averaged value, ρ is density, U is velocity, P is pressure, τ is viscous stress tensor, m_k is mass fraction of species k, J_k is diffusive flux of species k, and u and m'_k are fluctuating flow velocity and mass fraction of species k, respectively. Time averaging of the basic governing equations of flow processes leads to the appearance of apparent stress gradients ($\rho\overline{u}\overline{u}$) and mass transfer fluxes ($\rho\overline{u m'_k}$) associated with turbulent motion. The main challenge in modeling turbulent flow lies in the specification of these turbulent stresses and mass fluxes in terms of the time-averaged variables. Generally, for most engineering flow modeling applications, this so-called closure problem is solved by introducing a turbulence model. Several turbulence models have been proposed in the open literature [25,26], but unfortunately, there is none that can be used universally. Proper turbulence models need to be selected according to the problem under consideration.

This investigation intended to evaluate CFD modeling of mass transfer in annular reactors over a broad range of hydrodynamic conditions. The Reynolds number (Re) range analyzed was between 500 and 11,000, in which laminar, transitional and turbulent flow regimes were present. For the simulations having 500 < Re < 2100, the laminar hydrodynamic model was used, whereas for those simulations with 2100 < Re < 11,000 four different turbulence models were evaluated. In the first place, the widely used standard k–ε model (S k–ε) [27] was evaluated. Then, based on the results obtained by Sozzi and Taghipour [23], the realizable k–ε model (R k–ε) [28] and the Reynolds stress model (RSM) [29] were chosen for evaluation. Finally, the low Reynolds number turbulence model developed by Abe, Kondoh and Nagamo (AKN) [30] was selected for evaluation. This later model was chosen based on the successful predictions of mass and heat transfer obtained by other researchers in similar systems such as pipe expansions, turbulent pipes and impinging jets [31–33]. The five hydrodynamic models are briefly discussed in the following section.

2.2. Hydrodynamic models

2.2.1. Laminar model

When modeling laminar flow, identical equations to (13) and (14), but excluding the apparent stress gradients ($\rho\overline{u}\overline{u}$) associated with turbulent motion, need to be solved. These equations combined with the Newton's law of viscosity, as a constitutive equation to relate the stress tensor to the motion of the continuous fluid, allow computing the velocity field within the reactor. Further details and solved examples for this model can be found in Bird et al. [34].

2.2.2. Standard k-ε model (S k-ε)

The S k–ε model is a two-equation eddy viscosity model which is based on the Boussinesq hypothesis (approximation). The Boussinesq hypothesis makes the assumption that the Reynolds stresses can be expressed in terms of mean velocity gradients and that the turbulent eddy viscosity is related to the turbulence kinetic energy k and the dissipation rate ε. The advantage of this approach is the relatively low computational cost associated with the computation of the turbulent viscosity; however, it also presents the disadvantage of assuming the turbulent viscosity as an isotropic scalar quantity, which is not strictly true. The S k–ε model has proved reasonably accurate for many flows without highly curved streamlines or significant swirl. It usually underestimates flow separation and overestimates turbulence production by normal straining [35]. In the derivation of the model, the flow is assumed fully turbulent, and the effects of molecular viscosity are neglected. These assumptions therefore make the S k–ε model valid only for fully turbulent flows. Nonetheless, this turbulence model has been one of the most widely validated and used in engineering applications. The S k-ε model is described by Launder and Spaulding [27].

2.2.3. Realizable k–ε model (R k–ε)

The R k–ε model is a modification of the S k–ε model which incorporates a new formulation for the turbulent viscosity and a new transport equation for the dissipation rate ε. A benefit of the R k–ε model, compared with the S k–ε model, is that it predicts more accurately the spreading rate of planar and round jets, and it is also likely to provide superior performance for flows involving rotation, boundary layers under strong adverse pressure gradients, separation, and recirculation [36]. The details of this turbulence model can be found in Shih, et al. [28].

2.2.4. Reynolds stress model (RSM)

The RSM is the most elaborate turbulence model among the RANS based models. It does not use the Boussinesq hypothesis and rather than assuming isotropic turbulent viscosity, the RSM closes the RANS equations by solving individual transport equations for the Reynolds stresses, together with an equation for the dissipation rate. This turbulence model should be considered whenever non-isotropic effects are important; for example, in flows with strong curvature, swirling flows, and flows with strong acceleration/retardation. The fidelity of RSM predictions is still limited by the closure assumptions employed to model various terms in the exact transport equations for the Reynolds stresses. The modeling of the pressure–strain and dissipation-rate terms is particularly challenging, and often considered to be responsible for compromising the accuracy of RSM predictions [36]. Among some of the disadvantages of the RSM, Ranade [24] mentions that the model is computationally expensive, that it performs as poor as the k–ε model in some flows due to problems with the dissipation rate equation, and that it has not been widely validated yet. Launder et al. [29] present details of the RSM.

2.2.5. Enhanced wall treatment

The S k–ε, R k–ε, and RSM models are primarily valid for turbulent core flows (i.e., the flow in the regions somewhat far from walls). Therefore, special consideration needs to be given as to how to make these models suitable for wall-bounded flows. There are two main approaches to modeling the near-wall region. In one approach, the so-called 'wall function' approach, the viscosity-affected inner regions (viscous and buffer layers) are not modeled; instead, semi-empirical formulae (wall functions) are used to bridge the viscosity-affected region between the wall and the fully turbulent region [24]. This approach, although less memory and CPU intensive, misses important features of the mass transfer boundary layer if it is deeply embedded within the viscous sublayer. This situation makes the wall function approach inappropriate when modeling wall-mass or heat transfer in liquid flows. In the other approach, special low Reynolds number turbulence models

are developed to simulate the near-wall region flow, allowing for extending the turbulence model all the way to the wall [37,38]. This latter approach has given the best results when modeling wall mass and heat transfer, and thus it is the recommended method in these applications. In this investigation, when the S k–ε, R k-ε or RSM models were used to perform CFD simulations, the enhanced wall treatment available in the commercial CFD software was enabled. This treatment is a near-wall modeling method that combines a two-layer model applicable in regions with fine near-wall meshes, with enhanced wall functions used in regions with coarse meshes. When using the enhanced wall treatment, it is necessary thus to construct a proper fine mesh where the viscosity-affected near-wall region is desired to be fully resolved. Details of this method can be found in Fluent-Inc. [36].

2.2.6. AKN low Reynolds number turbulence model

Over the past few years, low Reynolds number (LRN) k–ε models have been widely used to predict wall-bounded flows due to their simplicity and capability of predicting the near wall flow, so as mass and heat transfers [39–41]. The low Reynolds number k–ε modeling approach incorporates either a wall-damping effect or a direct effect of molecular viscosity, or both, on the empirical constants and functions in the turbulence transport equations. This approach enables the extension of the k–ε turbulence model all the way to the wall. The low Reynolds number does not refer to the global Reynolds number, but the local turbulent Reynolds number formed by a turbulent fluctuation and turbulent length scale. This Reynolds number varies throughout the computational domain and is proportional to the ratio of the turbulent and physical viscosity [42]. Fairly complete reviews of low Reynolds number k–ε models have been presented by Patel et al. [43], Hrenya et al. [44], and Thakre and Joshi [45,46].

Among many others, the AKN model has shown promising results in modeling near-wall heat and mass transfers [31–33]. Abe et al. [30] modified the Nagano and Tagawa [47] LRN k–ε turbulence model, suggesting the use of the Kolmogorov velocity scale instead of the friction velocity to account for the near-wall and LRN effects in both attached and detached flows. Doing so, the model improved the prediction of the flows with separation and reattachment [30].

2.3. Mass transfer models

2.3.1. Laminar flow

When modeling mass transfer under laminar flow regime, Eq. (15), excluding the mass transfer fluxes ($\rho\overline{um'_k}$) associated with turbulent motion, needs to be solved. The diffusive flux of species k can be estimated using Fick's first law of diffusion:

$$J_k = -D_m \nabla(\rho m_k) \tag{16}$$

where D_m is the molecular diffusivity of species k in the mixture. Substituting Eq. (16) in (15) with $(\rho\overline{um'_k}) = 0$, gives the convection–diffusion mass transfer equation for laminar flow:

$$\nabla \cdot (\rho U m_k) = \nabla \cdot (D_m \nabla(\rho m_k)) \tag{17}$$

2.3.2. Turbulent flow

The closure problem associated with the specification of the mass transfer fluxes ($\rho\overline{um'_k}$) associated with turbulent motion modeling has been typically solved by analogy to the linear approximation for the Reynolds stresses (or to Fick's first law of diffusion):

$$\rho\overline{um'_k} = -D_t \nabla(\rho\overline{m_k}) \tag{18}$$

where D_t is the so-called eddy (or turbulent) diffusivity for species concentration. Combining Eqs. (18) and (15) results in the convection–diffusion turbulent mass transfer equation applicable to our case:

$$\nabla \cdot (\rho\overline{U}\overline{m_k}) = \nabla \cdot \left[\left(\rho D_m + \frac{\mu_t}{Sc_t}\right)\nabla\overline{m_k}\right] \tag{19}$$

with μ_t the turbulent viscosity and Sc_t the turbulent Schmidt number defined as the ratio between the turbulent viscosity and the turbulent diffusion:

$$Sc_t = \frac{\mu_t}{\rho D_t} \tag{20}$$

This dimensionless number typically is close to unity. Koeltzsch [48] reviewed the previous experimental investigations and found that most authors use a constant for Sc_t ranging from 0.5 to 0.9. In this investigation a value of 0.7 was used as recommended in various references [36,49,50]. The assumption of using a constant turbulent Schmidt number across the whole flow field has been questioned recently and some researchers have elaborated models that consider the dependence of Sc_t on global quantities of the flow [51], or as algebraic turbulence models [52]. More accurate predictions of mass and heat transfer have been reported using this approach [37,53]. Also, more complex models for solving the turbulent mass transfer equation have been recently proposed, like the two-equation model of B.T.Liu [54].

2.4. Geometrical models

The two model annular reactor geometries studied in the present work are shown in Fig. 1. Both reactors share the same main dimensions: 33 mm outer tube diameter, 21 mm inner tube diameter, 295 mm total length, 12 mm inlet and outlet diameter tubes. The inlet and outlet ports of the U-shape reactor were placed 20 mm from each respective end, so as the outlet port of the L-shape reactor. The inlet port of the L-shape reactor was centered on the front plate. The inlet and outlet tubes were chosen to be

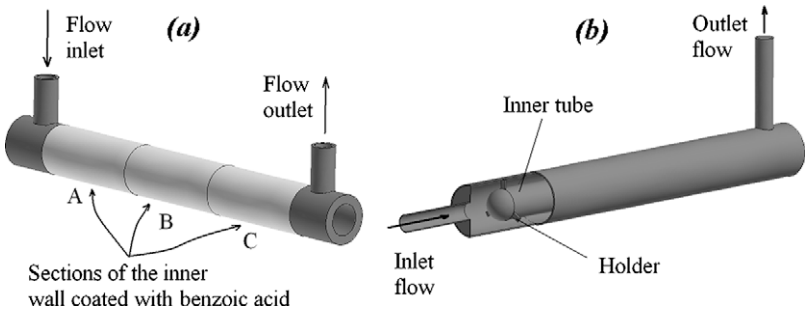

Fig. 1. Schematic diagram of the U-shape (a) and L-shape (b) annular reactors. The schematic of the U-shape reactor indicates the inner wall sections coded as A, B and C. The L-shape reactor is illustrated with a partial cut-off to show the inner tube with its holder.

at least 45 diameters in length to ensure that a fully developed flow was established at the entrance of the reactor and at the outlet boundary. The L-shape reactor inner tube began 20 mm away from the front plate and its holder was placed 30 mm from the front plate. The holder consisted of three prongs (3 mm wide × 6 mm long × 3 mm thick) located 120° one from another. Both annular reactors had three sections on the inner wall of the outer tube that could be set at constant concentration. Experimentally, this condition was achieved by depositing a benzoic acid coating onto the inner walls. This feature allowed for studying the mass transfer process at different regions along the annular volume of the reactors. Each section was 76 mm long and they were coded as follows: A for the inlet section, B for the middle section, and C for the outlet section.

2.5. Mesh design

When modeling turbulent mass transfer from a wall using the enhanced wall treatment or the low Reynolds number turbulence model approaches, it is fundamental to have a mesh fine enough that allows solving the governing equations all the way to the wall. Typical recommendations for being able to resolve the mean velocity and turbulent quantities in the near-wall region are to have a $y^+ \approx 1$ and at least 10 cells within the viscosity-affected near-wall region ($Re_y < 200$) [36]. Nevertheless, for high Schmidt number systems, the concentration boundary layer is much smaller than the velocity boundary layer. This fact makes it necessary to have even finer meshes within the near-wall region in order to be able to solve properly the concentration profiles. To define the mesh requirements in the sections of the reactor geometry where mass transfer from the wall was taking place, a preliminary study was performed. In this study, simulations of mass transfer in a straight pipe (10 mm diameter × 1 m long) with its internal wall coated with benzoic acid, and therefore at constant concentration, were performed. The four turbulence models (S k–ε, R k–ε, RSM and AKN) were evaluated. Eleven different meshes for the pipe operating under three water flow rates (Re = 7500, 35,000, 75,000) were evaluated not only in terms of mesh independent results, but also in terms of result accuracy. The benzoic acid outlet concentrations computed by the CFD simulation were compared with the predictions of the empirical correlation obtained by Harriott and Hamilton [55], which is reported to have an average deviation of 5.4% from the experimental data. The conclusions of the simulations under the three different water flow rates were basically the same; therefore, only some of the data corresponding to Re = 7500 are presented in Table 2 as the representative results. The results showed that a y^+ smaller than 0.5 at the wall-adjacent cell and at least 10 cells within the viscosity-affected near-wall region ($Re_y < 200$) were needed to obtain consistent and accurate results. These near-wall mesh requirements were then utilized in all the simulations performed in this investigation. It is also worth highlighting that the computations using the RSM and the AKN models provided the closest agreement with the estimations of the empirical correlation.

Table 2
Difference (%) in the exit concentrations of benzoic acid predicted by the empirical correlation of Harriott and Hamilton [55] and the CFD simulations.

Mesh	#1	#2	#3	#4	#5	#6
y^+	0.06	0.13	0.25	0.25	0.5	1.3
# cells $Re_y < 200$	19	14	19	15	14	11
RSM% error	2.5	3.9	1.8	2.8	1.4	23.8
AKN% error	4.3	5.1	3.1	3.3	6.8	31.1
R k-ε% error	17.7	17.6	17.4	17.7	14.4	33.5
S k–ε% error	17.7	18.4	17.4	18.0	14.4	33.9

Four different turbulence models and several near-wall meshes were evaluated.

The commercial mesh generator Gambit® was used to create the grid. For the case of the U-shape reactor, structured hexahedral cells were used to discretise the entire physical domain, whereas for the L-shape reactor it was necessary to split the reactor domain and use unstructured cells in the region where the inner tube holder was located (see Fig. 2(a)). For the annular region, where the mass transfer took place, a boundary-layer mesh accomplishing a $y^+ < 0.5$ and having at least 10 cells within the viscosity-affected near-wall region was setup (see Fig. 2(b)). The utilized grids for both reactors had approximately 1.3 million volume cells and they were verified to give mesh-independent results.

2.6. Boundary conditions

The boundary conditions for the CFD model were defined as follows. At the inlet, the mass flow rate of the fluid was specified. The direction of the flow was defined normal to the boundary. The hydraulic diameter was fixed at 12 mm and the turbulence intensity (TI) was set with values close to 5%. The turbulence intensity was estimated for each case based on the formula $TI = 0.16\ Re^{-1/8}$. This formula calculates the turbulence intensity at the core of fully developed flows [36]. At the outlet, a fully developed flow (outflow) condition was applied. At all the walls, a no-slip boundary condition was imposed. Also, zero diffusive flux of species was specified at the wall, except for the walls coated with benzoic acid, where a constant concentration of 3.4×10^{-3} (mass fraction) was fixed. This concentration corresponds to the saturation concentration of benzoic acid in water at 298 K [56].

2.7. Physical properties

The physicochemical process studied in this investigation is the isothermal convective mass transfer of benzoic acid in water at 298 K. Because at this temperature the saturation concentration of benzoic acid in water is very low, the physical properties of water can be assumed for the system. At 298 K the viscosity and the density of water are 8.9×10^{-4} Pa·s and 997 kg/m^3 respectively [57]. The assumed diffusion coefficient of benzoic acid in water was 9.32×10^{-10} m^2/s, which is the integral diffusion coefficient computed by Noulty and Lealst [58] over the concentration range from zero to saturation.

2.8. Numerical solution method and strategy

Commercial CFD code Fluent® 6.3.26 was used to perform the simulations. Fluent® has the S k–ε, R k–ε and RSM turbulence models, as well as six LRN models, among them being the AKN model. The AKN model constants were set to the software's default values which are identical to those in the high Reynolds number S k–ε model. Some researchers have found out that using this set of constants the model performs better [32].

The segregated steady-state solver was used to solve the governing equations. Second order upwind discretization scheme was employed except for pressure for which PRESTO! was selected. The SIMPLE algorithm was chosen for the pressure–velocity coupling. Convergence of the numerical solution was ensured by monitoring the scaled residuals to a criterion of at least 10^{-4} for the continuity and momentum variables, and 10^{-6} for the concentration. Additionally, the variation of velocity magnitude at one point of the computational domain located in an area of high velocity gradients was used as indicator of convergence.

Taking advantage of the fact that the very low concentrations of benzoic acid did not affect the velocity field within the reactor, the CFD model was solved in two steps. First, equations of continuity

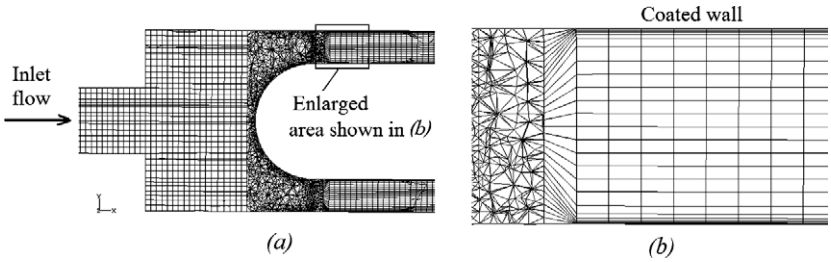

Fig. 2. Sections of the mesh used in the L-shape reactor: (a) longitudinal cut of the entrance zone where an unstructured mesh was required in the region of the inner tube holder and (b) enlargement of the annular region where a boundary-layer mesh is utilized.

(13) and motion (14) were solved for getting the flow field across the computational domain. Then, the velocity values were kept "frozen" and the equation of conservation of species (15) was solved using the converged flow solution. This solving strategy saves computation time and brings stability to the solution.

3. Experimental setup and procedure

The experimental work focused to generate data of the external mass transfer in both (U-shape and L-shape) annular reactors under different hydrodynamic conditions. The U-shape and L-shape annular reactors described in Section 2.4 were used in the experiments. The main reactor structure was made of PVC and included a union that allowed for setting up either reactor configuration as needed (see Fig. 3(a)). The coatings of benzoic acid, as a model chemical, were deposited on glass tubes (76 mm long and 33 mm inner diameter) with an outer diameter slightly smaller than the inner diameter of the PVC unit, so that the glass tubes could fit inside the PVC structure (see Fig. 3(b)). The coated glass tubes could be located at positions A, B or C as indicated in Fig. 1. When only one of the sections was desired to be coated with benzoic acid, two more glass tubes without any coating were placed at the other two positions. The glass tubes were coated by dipping them into molten benzoic acid (Fisher Scientific certified ACS). On contact with the cold glass, the benzoic acid solidified immediately, yielding a layer of the organic acid that presented a smooth and uniform appearance. Because the coating was desired only on the inner wall of the tubes, the outer walls and the borders were cleaned of the solidified acid using a sharp blade and then a wet cloth. The mass transfer rate was quantified in terms of the average mass transfer coefficient and was obtained by operating the reactors in recirculated batch mode using the experimental setup shown schematically in Fig. 4. The operation of the system involved recycling a constant flow rate of water at 25 °C into the reactor causing the dissolution of the slightly soluble benzoic acid into the bulk fluid. The coated tubes were used as long as a smooth layer of benzoic acid layer was present and covered all the internal surface of the tubes. The concentration of benzoic acid was monitored over time and determined via a UV spectrophotometer (UV-Mini 1240, Shimadzu) at 231 nm or 271 nm depending on the concentration range.

A mass balance of benzoic acid in the solution gives the following equation for the variation of the concentration with respect to time in the system:

$$C = C_{sat} + (C_0 - C_{sat})e^{-\frac{h_m A}{V}t} \tag{21}$$

where C is the concentration of benzoic acid in the mixed tank, C_{sat} is the saturation concentration of benzoic acid in water, C_0 is the concentration of the acid at $t = 0$, h_m is the average mass transfer coefficient, A is the area of mass transfer, V is the total volume of liquid and t is the elapsed time. Using a non-linear regression method for fitting the concentration versus time data, the average mass transfer coefficients were estimated. Flow rates of 1.2, 3.4, 6.6, 8.5, 11.4, 18.0 and 24.6 L/min were used, representing a range of Reynolds numbers of approximately $500 < Re < 11{,}000$ (based on the annulus of the reactor). The total volume of liquid used in the system was 15.0 L of distilled water. For each flow rate, the average mass transfer coefficient was determined by triplicate runs. Each of the following configurations were studied in both reactors: coating of benzoic acid in all sections A, B and C (A + B + C); only section A (A) coated; only section B (B) coated; only section C (C) coated.

4. Results and discussion

4.1. Mass transfer experimental results

The benzoic acid concentration versus time data obtained in the recirculated batch system were fitted to the model given by Eq. (21) utilizing a non-linear regression method, from which the average mass transfer coefficients of the system were estimated. The model fit the experimental data closely, presenting correlation coefficients > 0.999 and standard errors for the mass transfer coefficients <2%. The average mass transfer coefficients obtained for both reactor types operated under various hydrodynamic conditions and coating configurations are presented in Fig. 5. As

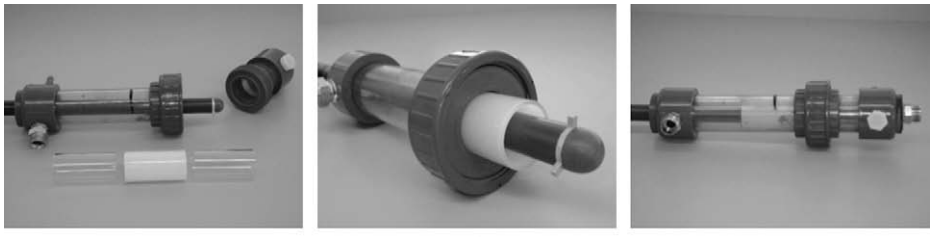

Fig. 3. L-shape annular reactor used in the experiments: (a) disarmed PVC structure with glass tubes next to it. The inner wall of the glass tube located in the middle is coated with benzoic acid, (b) coated glass tube fitted in the PVC structure and (c) armed PVC structure with the coated glass tube placed at position B.

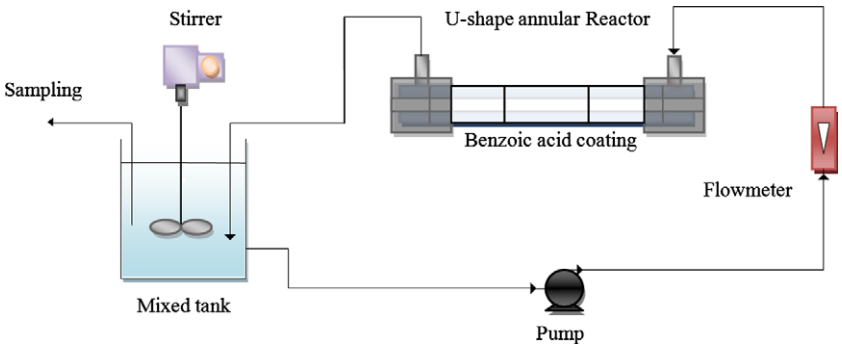

Fig. 4. Schematic of the recirculated batch annular reactor system used for determining the average mass transfer coefficients.

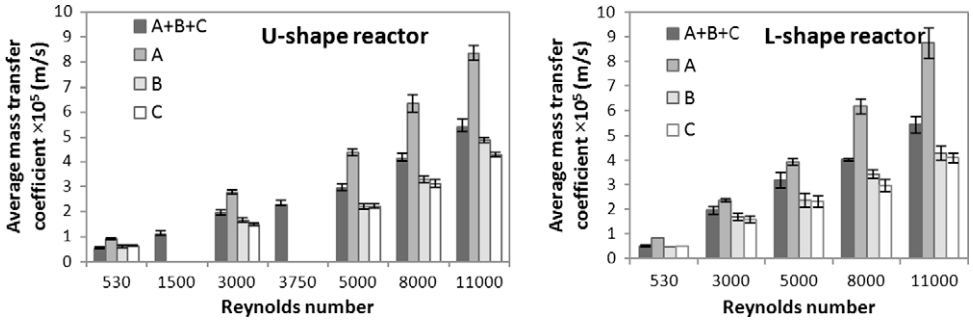

Fig. 5. Average mass transfer coefficients obtained for the U-shape and L-shape annular reactors operating under different hydrodynamic conditions. A, B and C indicate the sections coated with benzoic acid. The error bars represent the standard deviation obtained with triplicate runs.

expected, mass transfer coefficients increased monotonically with flow rates. For both reactor configurations the average mass transfer coefficients in section A were much higher than those in sections B, and those in section B were in turn slightly higher than the ones in section C. Mass transfer coefficient in section A was nearly twice that of sections B and C indicating that more than half of the total mass transfer in the reactor happened in the first third of its volume. This result was the same for all the hydrodynamic conditions investigated ($500 < Re < 11{,}000$). An important result is that the values of the average mass transfer coefficients obtained at each of the different sections were very similar for both reactor types. This finding indicates that in terms of average mass transfer efficiency, both annular reactor configurations perform similarly and therefore, there is no particular advantage of one over the other.

The mass transfer data obtained in this work showed good agreement with those from other reported investigations where similar annular configurations were used. Fig. 6 compares the average mass transfer coefficients obtained for transitional and turbulent flows ($3000 < Re < 11{,}000$) with the values predicted by the correlations tabulated in Table 1. The average mass transfer coefficients obtained in section A coincided well with the results calculated with the correlations corresponding to developing flow, in particular with Eqs. (22) and (23). The experimental data from sections B and C were in close agreement with the predictions of the correlations proposed for completely developed flow. These results suggest that the abrupt

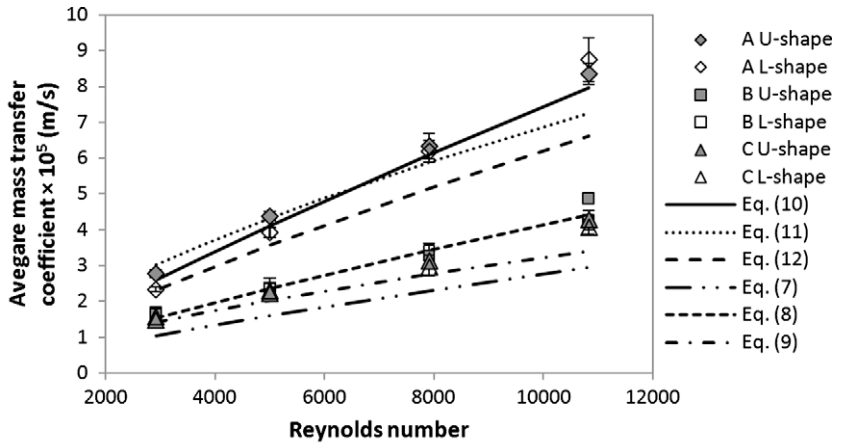

Fig. 6. Comparison of the average mass transfer coefficients obtained in the experiments with the ones estimated using different correlations reported in the literature. A, B and C indicate the sections coated with benzoic acid. The error bars represent the standard deviation obtained with triplicate runs.

expansion and change of direction that the fluid experiences at the inlet zone of both reactor geometries generate high turbulence, as well as a large near-surface concentration gradient, which results in high mass transfer in section A. The turbulence created in this region is then transported by convection and mass transfer decreases as the flow redevelops downstream of the entrance in sections B and C. Although not presented here, similar results were obtained for the laminar-flow data when compared with Eqs. (1)–(5).

4.2. CFD hydrodynamic simulations

CFD simulations of the annular reactors (U-shape and L-shape) operating at the same flow rates and conditions of the experiments were performed. From the perspective of hydrodynamic modeling, the inlet region of both annular reactors is the more challenging zone. The inlet flow impinges on the inner tube, from the top in the case of the U-shape reactor and from the front for the L-shape

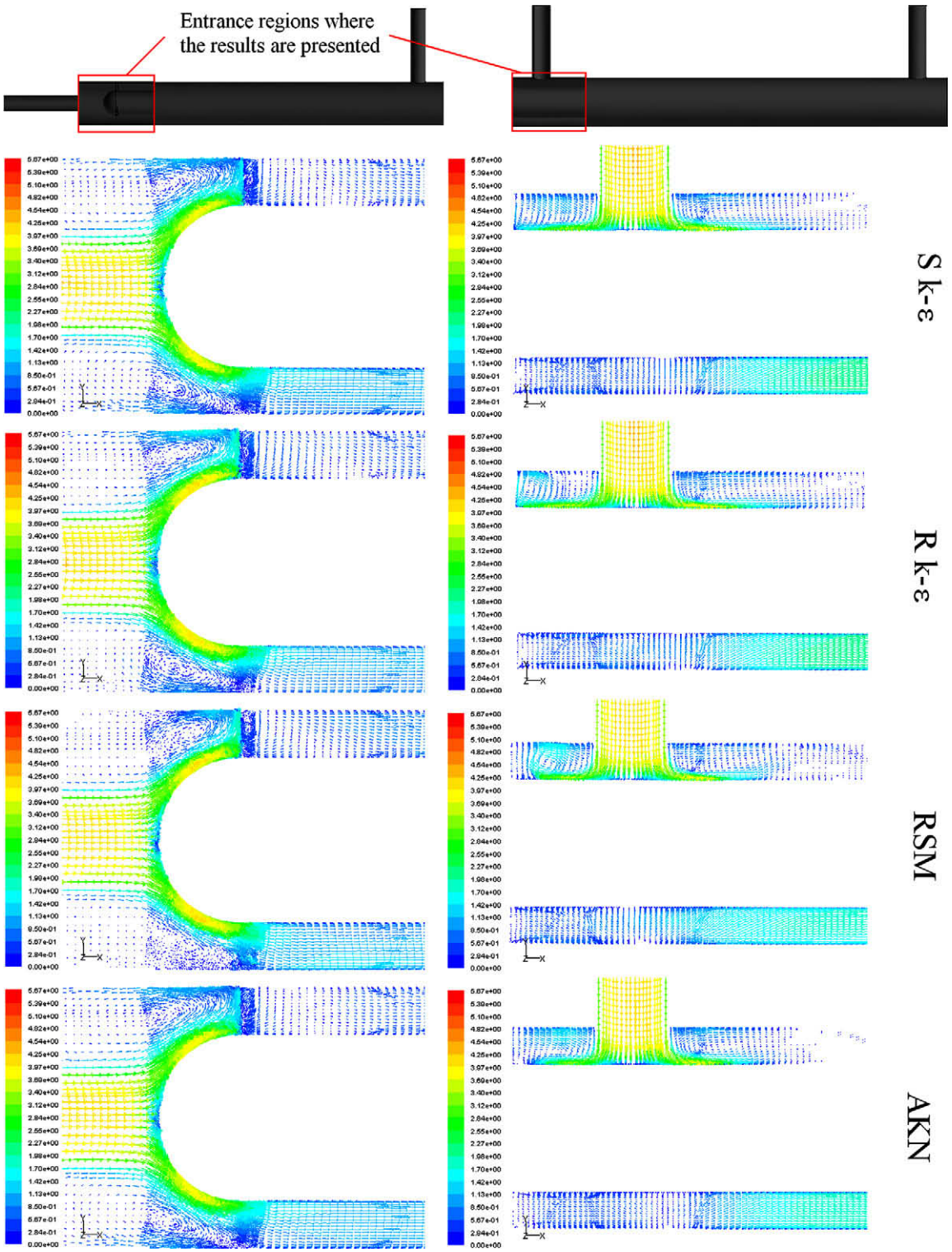

Fig. 7. Velocity vectors (m/s) on the longitudinal center plane at the inlet region of the L-shape (left) and U-shape (right) reactors using different turbulence models. The results correspond to a flow rate of 24.6 L/min (Re = 11,000).

configuration, causing the split of the flow and the creation of flow separation, recirculation, and reattachment zones. Fig. 7 shows the velocity vector field at the inlet regions of both reactors which were obtained from the simulations performed at a flow rate corresponding to Re = 11,000. The results correspond to the longitudinal center plane of the reactors. Similar velocity vector patterns were obtained in the simulations at the other flow rates. As it can be seen, the core velocity fields computed using the different turbulence models look somewhat similar. For example, all the simulations predicted the same recirculation zones, which in the case of the L-shape reactor were located at the entrance of the annular region (between the inner tube rounded end and the outer wall) and behind the holder prongs. The generation and location of such recirculation zones in similar reactor geometries were observed experimentally by Sozzi and Taghipour [23] using PIV techniques.

Fig. 8 shows the velocity magnitude contours along the U-shape and L-shape reactor volumes computed using the R k-ε turbulence model and for Re = 11000. The same flow patterns were also found when using the other turbulence models as well as for the other flow rates. As seen in Fig. 8, the velocity magnitude distribution along the annular space for the L-shape reactor is more uniform than that for the U-shape reactor. The U-shape reactor shows higher velocities in the section opposite the inlet and outlet ports (bottom of the reactor) and a low velocity region at the top. Such dissimilar velocity fields will produce very different local mass transfer at the walls of both reactor configurations (this topic is discussed further in Section 4.3). The veracity of these particular velocity distributions predicted by the CFD simulations was verified by letting the water flow in the reactors for a long time, so that the benzoic acid coatings were eroded by the stream at the regions of high velocity. The analysis of erosion patterns observed in both reactor configurations agreed with the CFD simulation predictions.

The previously analyzed results indicate that all the turbulence models under evaluation (S k–ε, R k–ε, RSM and AKN), indistinctly of the near-wall region model they utilized, were capable of somehow predicting the main characteristics of the core flow hydrodynamics within both annular reactors. However, accurate mass transfer prediction depends largely on the near-wall region flow modeling; consequently, the fact that a turbulence model can describe appropriately the core flow field does not guarantee its correct prediction of the surface mass transfer phenomenon. This subject matter will be analyzed in the following section.

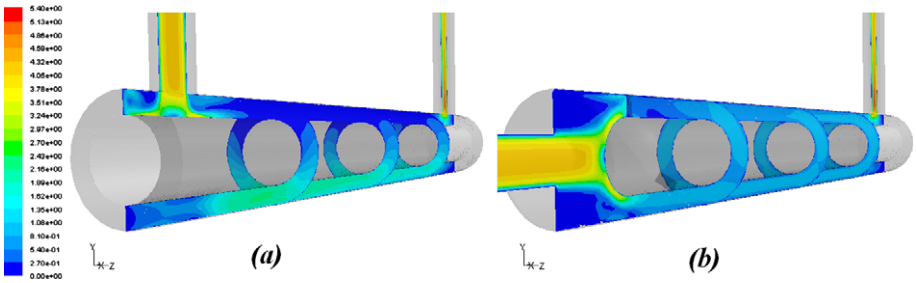

Fig. 8. Contours of velocity magnitude (m/s) in the U-shape (left) and L-shape (right) annular reactors calculated using the R k–ε model. The figure shows the longitudinal center plane and transversal planes at the middle of sections A, B and C. The results correspond to a flow rate of 24.6 L/min (Re = 11,000).

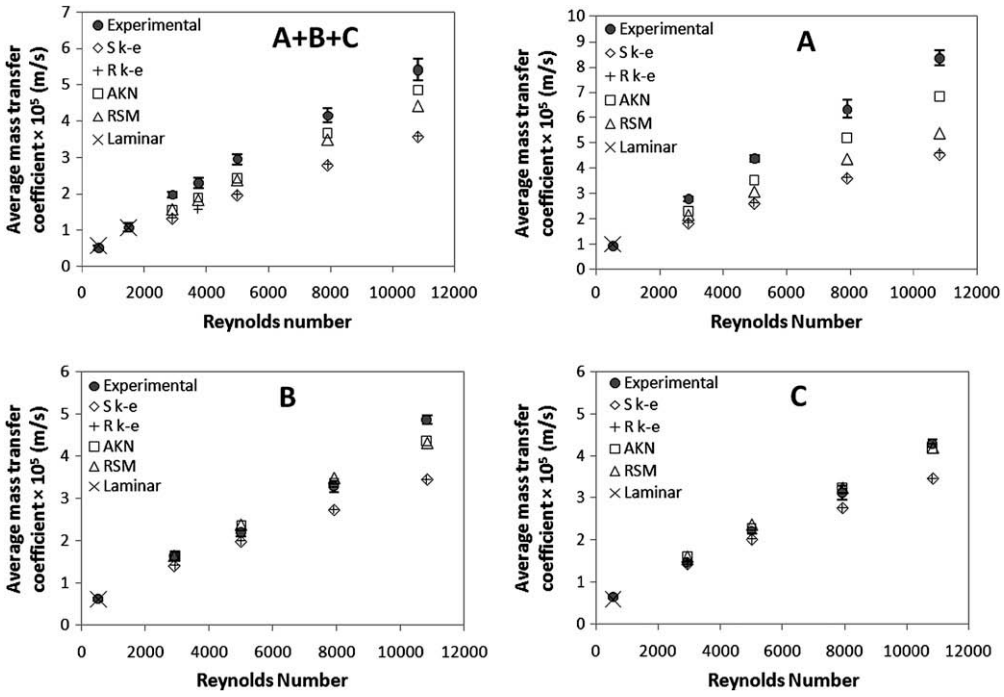

Fig. 9. Comparison of the average mass transfer coefficients obtained in the CFD simulations with the experimental values for the U-shape reactor. The results presented were obtained using different hydrodynamic models and at sections A, B and C of the reactor. The error bars represent the standard deviation obtained with triplicate runs.

4.3. Comparison of CFD mass transfer predictions with experimental data

Having the CFD simulation results obtained for different flow rates and hydrodynamic models, the corresponding average mass transfer coefficients in the reactors were calculated using:

$$h_m = \frac{Q}{A} \ln\left(\frac{C_{sat} - C_i}{C_{sat} - C_0}\right) \tag{22}$$

where Q is the flow rate, C_i and C_o are the concentrations of benzoic acid at the inlet and outlet of the reactor, respectively. Eq. (22) is obtained by performing a mass balance over the system, assuming that the concentration of benzoic acid at the wall is constant and corresponds to the saturation concentration of the acid in water. Fig. 9 presents the average mass transfer coefficients calculated using the CFD simulation results for the U-shape configuration. Also, the experimental results are presented for comparison with the CFD simulations. The results obtained for the L-shape annular configuration were very similar to those of the U-shape and therefore not shown here.

Fig. 9(a) shows the results corresponding to the case where mass transfer was taking place at all the sections (A + B + C). It can be seen that the results for laminar flow regimes showed excellent agreement with the predictions by the laminar model. However, all the evaluated turbulence models to some extent underestimated the global mass transfer rates associated with all the flow rates. The AKN predictions were the ones having the closest agreement with the experimental data (around 10% error), followed by those of the RSM. More insight on the capabilities of the turbulence models to predict mass transfer is obtained via the analysis of the results acquired for the individual sections (see Fig. 9(b)–(d)). All the turbulence models underestimated the mass transfer in section A, but the agreement between the results in sections B and C were quite close over the whole evaluation range ($3000 < Re < 11{,}000$). This result demonstrates that the disagreement found in the case corresponding to sections (A + B + C) is due to the underprediction computed by the turbulence models at section A. One possible reason for this discrepancy is that the turbulence models were not able to capture all the small eddies generated at the inlet, due to the sudden expansion of the flow. However, once the flow redeveloped through sections B and C, turbulence decreased and the models performed better.

Further investigation on the liquid-to-wall mass transfer predicting capabilities of the hydrodynamic and near-wall models was carried out by analyzing their ability to predict local mass transfer coefficients. A user defined function (UDF) for calculating the local mass transfer coefficient (h) at the wall of the reactors was programmed and integrated into the CFD model using the following equation:

$$h = \frac{D_m(C_{sat} - C_a)}{\delta(C_{sat} - C_b)} \tag{23}$$

where is C_a and C_b are the benzoic acid concentrations in the wall-adjacent cell and in the bulk of the fluid, respectively, and δ is the distance from the wall-adjacent-cell center to the wall. The three-dimensionality of the flow in the analyzed annular reactors, generated mainly by the specific inlet configurations, creates a two-dimensional local mass transfer distribution at the reactor wall. Fig. 10 shows the maps of local mass transfer coefficients in section A for both reactor configurations as computed utilizing the AKN model (Re = 11,000). In the case of the L-shape configuration, local mass transfer at the wall is more uniform; however, three regions of low mass transfer are evident behind each of the lamp holder prongs. The local mass transfer distribution in the U-shape reactor

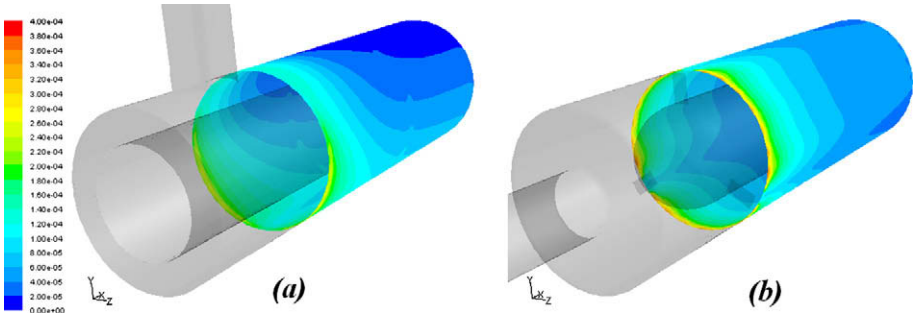

Fig. 10. Local mass transfer coefficient (m/s) distributions at entrance section A as computed using the AKN model and for a flow rate of 24.6 L/min (Re = 11,000): (a) U-shape, and (b) L-shape reactor configuration.

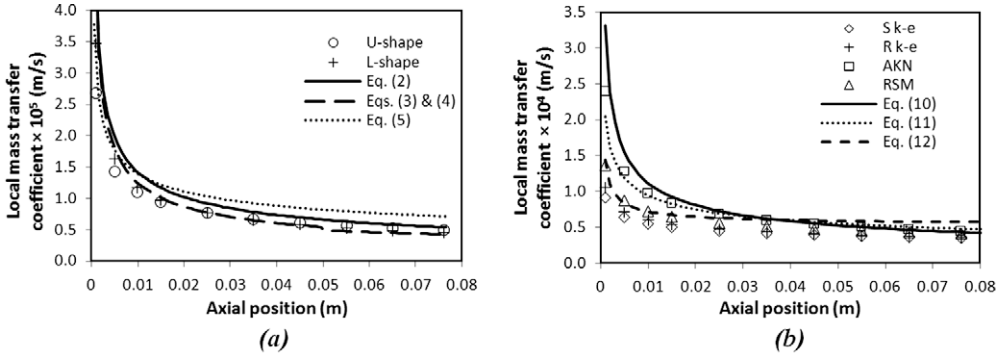

Fig. 11. CFD predictions of the local mass transfer coefficient along the reactor axis compare with values calculated from correlations: (a) Re = 530 and (b) Re = 11,000, L-shape configuration.

presents high values at the bottom and low values at the top of section A. These results are in accordance with the velocity field results obtained in Section 4.2, since higher mass transfer rates are expected in areas with higher fluid velocity gradients near the wall.

The most desirable way to evaluate these CFD simulations would be to compare the predictions with experimental measurements of local mass transfer throughout the walls. Unfortunately, such measurements were not within the scope of this work, nor there were any found in the open literature for the studied configurations. As a result, an alternative evaluation was performed utilizing the one-dimensional correlations reported in Table 1. From these correlations, a local mass transfer coefficient was calculated through differentiation according to:

$$h_x = \frac{d(h_m x)}{dx} \tag{24}$$

where x is the axial position. These data were compared with the average values at axial position x, calculated from the CFD-computed local mass transfer coefficients. The averaging was done around the circumference of the wall at each axial position (x). Fig. 11 presents the results obtained for both reactor configurations operating at Re = 530, and for the L-shape configuration operating at Re = 11,000. The results for the U-shape configuration and for other turbulent flow rates were similar and therefore not shown here.

As it can be seen in Fig. 11 (a), laminar CFD-computed local mass transfer coefficients were consistent with those calculated from the correlations, especially with the data of Ould-Rouis et al. [11]. Even though the different types of reactor inlets produced different local mass transfer distributions on the reactor wall (as shown in Fig. 10), the average values at an axial position x were not much different from one another. These results demonstrate the advantage of applying CFD modeling as it brings more insight into the analyzed system by providing the local mass transfer coefficient at each point; information which cannot be obtained from the correlations. For the predictions of the turbulence models, the results presented in Fig. 11 (b) show a better performance for the AKN model, followed by the RSM. AKN was able to predict higher local mass transfer coefficients in the entrance region and as a consequence, provided values closer to the data obtained from correlations (22) and (23). It should be noted that Eq. (22) had the closest agreement with the average mass transfer coefficients experimentally obtained in this work. For values of $x/d_e > 2$ ($x > 0.024$ m), the agreement with Eqs. (22) and (23) was excellent, but for values of $x/d_e < 2$ ($x < 0.024$ m) some underprediction with respect to Eq. (22) was found. Other investigations reported that the AKN model could successfully predict separating and reattaching flows downstream of a backward-facing step [30], so as liquid-to-wall mass transfer in pipes [32]. The analyzed L-shape annular reactor involves most of the essential physics of these two systems. Fig. 11 (b) also evidences that the difference in the predictions of the turbulence models happens in the entrance region. After $x/d_e > 5$ ($x > 0.06$ m) the predictions of all of the turbulence models are basically the same.

Overall, AKN model provided better mass transfer predictions, particularly in section A. Based on the hydrodynamic simulations and the experimental evidences obtained in this investigation, it was not possible to find any significant difference between the flow fields computed using any of the k–ε-based turbulence models. Consequently, the better performance of the AKN model might be explained in terms of the large impact that near-wall region modeling has on surface mass transfer predictions. In this sense, it appears that for the systems under investigation, the LRN approach simulates better the near-wall region than the two-layer approach employed in the enhanced wall treatment.

Table 3
Enhancement in the average mass transfer coefficient in section A due to perturbing flows created by the inlet sections.

Re	L-shape	U-shape
530	0.83	0.87
3000	1.25	1.22
5000	1.66	1.61
8000	1.89	1.83
11,000	2.02	1.96

Results correspond to the ratio between the mass transfer coefficients obtained with and without inlet ports as computed by laminar (Re = 530) and AKN (3000 < Re < 11,000) hydrodynamic models.

The effect of perturbing flows, created by the inlet sections, on the average mass transfer coefficients in section A was investigated utilizing the AKN model. The values computed for both reactor configurations were compared with the results obtained for a long (0.6 m) annular configuration without inlet/outlet ports. In this way, no extra phenomena, such as recirculation, or flow expansion/compression exist at the inlet/outlet boundaries. This configuration was achieved by defining a plug-flow at the inlet and a fully developed flow at the outlet as the boundary conditions in the model. The results are presented in Table 3 as the ratio between mass transfer coefficients with and without the inlet sections. For the transitional and turbulent flow conditions, the mass transfer enhances with Reynolds number due to the presence of inlet ports. At Re = 11,000 the average mass transfer coefficient in section A obtained with either a parallel or perpendicular inlet port is twice the value obtained without these ports. Interestingly, in the case of laminar flow, the mass transfer coefficient is lower when an inlet section is present. These results demonstrate the significant impact of the inlet section on the reactor overall mass transfer performance, so as the importance of considering the inlet/outlet ports when modeling commercial-type annular reactors.

5. Conclusions

In this study, experiments and CFD simulations were carried out in order to evaluate the accuracy of different hydrodynamic models for the prediction of surface mass transfer in annular reactors. Two common reactor configurations (U-shape and L-shape) were tested within a range of flow rates corresponding to 500 < Re < 11,000.

The experiments performed in both annular reactors revealed that half of the surface mass transfer took place near the entrance region of the reactor. Also, both annular reactors provided similar mass transfer efficiencies; indicating that there was no particular advantage for either configuration in terms of mass transfer. However, if erosion of the surface material (e.g. catalyst) is an issue, the L-shape reactor which provides a more uniform near-wall velocity gradient might be a better option.

The turbulence models under evaluation (S k–ε, R k–ε, RSM and AKN) predicted comparable core flow hydrodynamics which were in agreement with previous PIV investigations of similar systems. The mass transfer measurements demonstrated that the laminar model was able to predict successfully the mass transport in laminar flows. On the other hand, the AKN and the RSM models performed well and predicted turbulent mass transfer in both annular reactors, except for a moderate underestimation at the entrance region where high turbulence and mass transfer rates were found. For the case where the entire reactor was analyzed, the relative error of the estimations for the AKN and RSM models were approximately 10% and 20%, respectively. The predictions of both turbulence models were accurate within the entire range of flow rates investigated, which included flows under transitional regime.

Near-wall modeling was found to be critical in surface mass transfer simulations.

Inlet sections of annular reactors play an important role in the reactor hydrodynamics and consequently on its mass transfer performance. For that reason, these sections should be included in the annular reactor model.

The results obtained in this investigation make the AKN and RSM models very attractive for CFD-based simulations of turbulent annular reactors. The AKN model presents the advantage of being less memory and computational intensive than the RSM.

Acknowledgements

The authors acknowledge financial support from the Natural Sciences and Engineering Research Council of Canada (NSERC) and BI PureWater (Canada) Inc. J. Esteban Durán also thanks the Universidad de Costa Rica.

References

[1] A. Karim, J. Bravo, D. Gorm, T. Conant, A. Datye, Comparison of wall-coated and packed-bed reactors for steam reforming of methanol, Catal. Today 110 (2005) 86–91.
[2] F. Kapteijn, R.M. Deugd, J.A. Moulijn, Fischer–Tropsch synthesis using monolithic catalysts, Catal. Today 105 (2005) 350–356.
[3] H. Moueddeb, J. Sanchez, C. Bardot, M. Fick, Membrane bioreactor for lactic acid production, J. Membrane Sci. 114 (1996) 59–71.
[4] D.J. Pickett, Electrochemical Reactor Design, second ed., Elsevier Scientific Publishing Company, Amsterdam, 1979 (Chapter 4).
[5] M.L. Castro, F. Priego, N. Sanchez, Is dialysis alive as a membrane-based separation technique?, Trends Anal Chem. 27 (2008) 315–326.
[6] F. Taghipour, M. Mohseni, CFD simulation of UV photocatalytic reactors for air treatment, AIChE J. 51 (11) (2005) 3039–3047.
[7] V. Tomasic, F. Jovic, Z. Gomzi, Photocatalytic oxidation of toluene in the gas phase: modelling an annular photocatalytic reactor, Catal. Today 137 (2008) 350–356.
[8] B.N. Rai, A.K. Sinha, U.K. Ghosh, S.N. Gupta, S.N. Upadhyay, Force convective mass transfer in annuli, Chem. Eng. Commun. 68 (1988) 15–30.
[9] A.A. Mobarak, H.A. Farag, G.H. Sedahmed, Mass transfer in smooth and rough annular ducts under developing flow conditions, J. Appl. Electrochem. 27 (1997) 201–207.
[10] T. Ross, A. Wragg, Electrochemical mass transfer studies in annuli, Electrochim. Acta 10 (1965) 1093–1106.
[11] M. Ould-Rouis, A. Salem, J. Legrand, C. Nouar, Etude numérique et expérimentale des transferts de matière et de quantité de mouvement dans un écoulement annulaire laminaire non établi, Int. J. Heat Mass Transfer 38 (1995) 953–967.
[12] U. Ghosh, S. Upadhyay, Mass transfer to Newtonian and non-Newtonian fluids in short annuli, AIChE J. 31 (1985) 1721–1724.
[13] A. Bakker, A.H. Haidar, L.M. Oshinowo, Realize greater benefits from CFD, Chem. Eng. Process 97 (3) (2001) 45–53.
[14] J.L. Houzelot, J. Villermaux, Mass transfer in annular cylindrical reactors in laminar flow, Chem. Eng. Sci. 32 (1977) 1465–1470.
[15] D. Papadias, L. Edsberg, P. Björnbom, Effect of eccentricity and interaction between kinetics and mass transfer on the behaviour of catalytic annular reactors: a comparison between lumped and distributed models, Chem. Eng. Sci. 56 (2001) 4863–4878.
[16] S. Rodrigues de Farias, P. Legentilhomme, J. Legrand, Finite element simulation of mass transfer in laminar swirling decaying flow induced by means of a tangential inlet in an annulus, Comput. Methods Appl. Mech. Eng. 190 (2001) 4713–4731.
[17] G.E. Imoberdorf, A.E. Cassano, H.A. Irazoqui, O.M. Alfano, Optimal design and modeling of annular photocatalytic wall reactors, Catal. Today 129 (2007) 118–126.
[18] M. Maestri, A. Beretta, T. Faravelli, G. Groppi, E. Tronconi, Role of gas-phase chemistry in the rich combustion of H_2 and CO over a Rh/Al_2O_3 catalyst in annular reactor, Chem. Eng. Sci. 62 (2007) 4992–4997.
[19] J. Legrand, P. Legentilhomme, S.F. Neto, H. Aouabed, Mass transfer in developing flows, Electrochim. Acta 42 (1997) 805–811.
[20] J. Legrand, S.A. Martemyanov, Turbulent mass transfer in small radius ratio annuli, J. Appl. Electrochem. 24 (1994) 737–744.
[21] S. Martemyanov, E. Skurygin, J. Legrand, Turbulent mass transfer in the developing diffusion layer at large Schmidt numbers, Int. J. Heat Mass Transfer 42 (1999) 2357–2362.
[22] M. Mohseni, F. Taghipour, Experimental and CFD analysis of photocatalytic gas phase vinyl chloride (VC) oxidation, Chem. Eng. Sci. 59 (7) (2004) 0609–1601.
[23] D.A. Sozzi, F. Taghipour, Computational and experimental study of annular photo-reactor hydrodynamics, Int. J. Heat Fluid Flow 27 (6) (2006) 1043–1053.
[24] V.V. Ranade, Computational Flow Modeling for Chemical Reaction Engineering, Academic Press, London, 2002 (Chapter 3).
[25] M. Nallasamy, Turbulence models and their applications to the prediction of internal flows: a review, Comput. Fluids 15 (2) (1987) 151–194.
[26] D.C. Wilcox, Turbulence Modeling for CFD, DCW Industries, La Cañada, Calif, 2006 (Chapter 4).
[27] B.E. Launder, D.B. Spalding, The numerical computation of turbulent flows, Comput. Methods Appl. Mech. Eng. 3 (1974) 269–289.
[28] T.H. Shih, W.W. Liou, A. Shabbir, Z. Yang, J. Zhu, A new k–ε eddy viscosity model for high Reynolds number turbulent flows: model development and validation, Comput. Fluids 24 (1995) 227–238.
[29] B.E. Launder, G.J. Reece, W. Rodi, Progress in the development of a Reynolds-stress turbulence closure, J. Fluid Mech. 68 (1975) 537–566.
[30] K. Abe, T. Kondoh, Y. Nagano, A new turbulence model for predicting fluid flow and heat transfer in separating and reattaching flows: I. Flow field calculations, Int. J. Heat Mass Transfer 37 (1) (1994) 139–151.
[31] W.D. Hsieh, K.C. Chang, Calculation of wall heat transfer in pipe-expansion turbulent flows, Int. J. Heat Mass Transfer 39 (18) (1996) 3813–3822.
[32] Y. Wang, J. Postlethwaite, D.J. Bergstrom, Modelling mass transfer entrance lengths in turbulent pipe-flow with applications to small cathodes for measuring local mass transfer rates, J. Appl. Electrochem. 26 (1996) 471–479.
[33] S.J. Wang, A.S. Mujumdar, A comparative study of five low Reynolds number k–ε models for impingement heat transfer, Appl. Therm. Eng. 25 (2005) 31–44.
[34] R.B. Bird, W.E. Stewart, E.N. Lightfoot, Transport Phenomena, second ed., John Wiley & Sons, New York, 2002 (Chapter 2).
[35] R.H. Perry, D.W. Green, Perry's Chemical Engineers' Handbook, seventh ed., McGraw-Hill, New York, 1997. pp. 6.45–6.47.
[36] Fluent-Inc., FLUENT 6.3 User's Guide, Modeling Turbulence, Lebanon, NH, 2006 (Chapter 12).
[37] M. Wolfstein, The velocity and temperature distribution of one-dimensional flow with turbulence augmentation and pressure gradient, Int. J. Heat Mass Transfer 12 (1969) 301–318.
[38] W.P. Jones, B.E. Launder, The prediction of laminarization with a two-equation model of turbulence, Int. J. Heat Mass Transfer 15 (1972) 301–314.
[39] M.T. Dhotre, J.B. Joshi, CFD simulation of heat transfer in turbulent pipe flow, Ind. Eng. Chem. Res. 43 (2004) 2816–2829.
[40] Y. Wang, J. Postlethwaite, The application of low Reynolds number k–ε turbulence model to corrosion modelling in the mass transfer entrance region, Corros. Sci. 39 (7) (1997) 1265–1283.
[41] S. Nesic, G. Adamopoulos, J. Postlethwaite, D.J. Bergstrom, Modelling of turbulent flow and mass transfer with wall function and low-Reynolds number closures, Can. J Chem. Eng. 71 (1993) 28–34.
[42] L. Davidson, An Introduction to Turbulence Models, Chalmers University of Technology, Sweden, 2003 (Chapter 4).
[43] V.C. Patel, W. Rodi, G. Scheuerer, Turbulence models for near wall and low Reynolds number flows: a review, AIAA J 23 (1984) 1308–1319.
[44] C.M. Hrenya, E.J. Boilo, D. Chakrabarti, J.L. Sinclair, Comparison of low Reynolds number k–ε turbulence model in predicting fully developed pipe flow, Chem. Eng. Sci. 50 (12) (1995) 1923–1941.
[45] S.S. Thakre, J.B. Joshi, CFD modeling of heat transfer in turbulent pipe flows, AIChE J. 46 (9) (2000) 1798–1812.
[46] S.S. Thakre, J.B. Joshi, Momentum mass and heat transfer in single phase turbulent flow, Rev. Chem. Eng. 18 (2002) 83–293.
[47] Y. Nagano, M. Tagawa, An improved k–ε model in boundary layer flows, J.Fluids Eng. 112 (1990) 33–39.
[48] K. Koeltzsch, The height dependence of the turbulent Schmidt number within the boundary layer, Atmos. Environ. 34 (2000) 1147–1151.
[49] I. Yimer, I. Campbel, L-Y. Jiang, Estimation of the turbulent Schmidt number from experimental profiles of axial velocity and concentration for high-Reynolds-number jet flows, Can. Aeronautics Space J. 48 (3) (2002) 195–200.
[50] D.B. Spalding, Concentration fluctuations in a round turbulent free jet, Chem. Eng. Sci. 26 (1971) 95–107.
[51] C. Rosen, C. Traegaardh, Prediction of turbulence high Schmidt number mass transfer using a low Reynolds number k–ε turbulence model, Chem. Eng. J. 59 (1995) 153–159.
[52] S. Aravinth, Prediction of heat and mass transfer for fully developed turbulent fluid flow through tubes, Int. J. Heat Mass Transfer 43 (2000) 1399–1408.
[53] G. Nelissen, B. van den Bossche, J. Deconinck, A. van Theemsche, C. Dan, Laminar and turbulent mass transfer simulations in a parallel plate reactor, J. Appl. Electrochem. 33 (2003) 863–873.
[54] Z.M. Sun, B.T. Liu, X.G. Yuan, C.J. Liu, K.T. Yu, New turbulent model for computational mass transfer and its application to a commercial-scale distillation column, Ind. Eng. Chem. Res. 44 (2005) 4427–4434.
[55] P. Harriott, R.M. Hamilton, Solid–liquid mass transfer in turbulent pipe flow, Chem. Eng. Sci. 20 (1965) 1073–1078.
[56] R.E. Kirk, D.F. Othmer, Kirk–Othmer Encyclopedia of Chemical Technology, vol. 3, John Wiley & Sons, Inc, New Jersey, 2001. p. 626.
[57] D.R. Lide, CRC Handbook of Chemistry and Physics, 88th ed., CRC, Boca Raton, 2007. p. 6.2.
[58] R.A. Noulty, D.G. Lealst, Diffusion coefficient of aqueous benzoic acid at 25 °C, J. Chem. Eng. Data 32 (1987) 418–420.